Research Article
Biomedical Optics EXPRESS

# Evaluation of a transparent cranial implant as a permanent window for cerebral blood flow imaging

NAMI DAVOODZADEH,[1] MILDRED S. CANO-VELÁZQUEZ,[2] DAVID L. HALANEY,[1] CARRIE R. JONAK,[3] DEVIN K. BINDER,[3] AND GUILLERMO AGUILAR[1]

[1]*Department of Mechanical Engineering, University of California, Riverside, CA, USA*
[2]*Instituto de Investigaciones en Materiales, Universidad Nacional Autónoma de México, México*
[3]*Division of Biomedical Sciences, School of Medicine, University of California, Riverside, CA, USA*
**gaguilar@engr.ucr.edu*

**Abstract:** Laser speckle imaging (LSI) of mouse cerebral blood flow was compared through a transparent nanocrystalline yttria-stabilized zirconia (nc-YSZ) cranial implant over time (at days 0, 14, and 28, n = 3 mice), and vs. LSI through native skull (at day 60, n = 1 mouse). The average sharpness of imaged vessels was found to remain stable, with relative change in sharpness under 7.69% ± 1.2% over 28 days. Through-implant images of vessels at day 60 appeared sharper and smaller on average, with microvessels clearly visible, compared to through-skull images where vessels appeared blurred and distorted. These results suggest that long-term imaging through this implant is feasible.



## 1. Introduction

Laser speckle imaging (LSI) is a widely used imaging technique which is capable of distinguishing between static and dynamic regions of a sample. Due to its high spatiotemporal resolution, this technique has proved useful for a range of applications such as object velocity measurements [1], blood flow sensing [2], laser vibrometry [3], surface roughness evaluation [4], and acousto-optic tomography [5, 6], as well as imaging blood flow [2, 7–21].

The first application of LSI to cerebral blood flow imaging [8] used LSI spatial contrast analysis [7]. Subsequently, LSI temporal contrast was developed [9, 10], which allowed for reduced static noise and improved spatial resolution compared to LSI spatial contrast analysis, at the expense of temporal resolution. In LSI temporal contrast imaging, a coherent source is directed onto a roughened surface, and the scattered light produces a random interference pattern called speckle [11, 12]. Movement of scattering particles within the random medium causes phase shifts in the scattered light and thus changes the random interference pattern, producing temporal fluctuations in the speckle pattern [11, 12]. When this speckle pattern is imaged with a camera of limited exposure time, these temporal fluctuations in the speckle pattern corresponding to dynamic regions of the sample appear smoother than the surrounding static regions [13, 22]. The degree of smoothness is measured as speckle contrast, and previous studies applying LSI to cerebral blood flow have shown that this speckle contrast correlates with blood flow velocity [11, 13].

This improved method of LSI temporal contrast imaging was applied to intact rat skull [14], but the poor transparency of the skull resulted in limited spatial resolution of the underlying blood flow. Previous studies have addressed this challenge in animal models by thinning [15] or polishing [16] the skull, optically clearing the skull [17], or by replacing a portion of skull with a transparent window made from glass or PDMS [23–25], which are powerful research techniques but which are not appropriate for human application as permanent cranial implants for patients. Skull thinning and polishing techniques affects

protection for the brain, glass-based windows have extremely low fracture toughness of typical glasses ($K_{IC}$ = 0.7-0.9 MPa $m^{1/2}$) [26] which increases potential for catastrophic failure by fracture, and the effect of skull optical clearing agents for long-term use on human skull is unknown. A number of biomedical considerations including biocompatibility, mechanical strength, and ageing should be examined in order to create an optical window for eventual clinical application. Conventional cranial prosthesis including titanium, alumina, and acrylic [27], have not provided the requisite combination of transparency and toughness required for clinically-viable transparent cranial implants. To address this challenge, our group has previously introduced a transparent nanocrystalline yttria-stabilized-zirconia cranial implant material, which possesses the mechanical strength and biocompatibility which are prerequisites for a clinically-viable permanent cranial implant for patients [28–30]. Yttria-stabilized zirconia (YSZ) represents an attractive alternative, due to its relatively high toughness ($K_{IC}$ ~8 MPa $m^{1/2}$) [31], as well as its proven biocompatibility in dental and orthopedic applications [32–34].

We have previously shown that this implant, which we refer to as the "Window to the Brain" implant (WttB), allows for increased imaging depth and contrast compared to the native skull for optical coherence tomography (OCT) [28] as well as ultrasound [35]. In this present study, we sought to expand upon previous indications that this WttB implant allows for improved LSI spatial resolution of brain blood flow compared to imaging through the native skull in mice [36]. Specifically, we investigate the stability of the WttB implant for LSI temporal contrast imaging by comparing the sharpness of mouse cerebral blood flow images over 28 days. We also compare LSI temporal contrast imaging between the WttB implant and native skull in a long-term mouse at 60 days post-implantation.

## 2. Methods

### *2.1 Implant fabrication and preparation*

Transparent nanocrystalline 8 mol% $YO_{1.5}$ yttria-stabilized zirconia (nc-YSZ) implant samples were produced from a precursor YSZ nanopowder (Tosoh USA, Inc., Grove City, OH, USA) densified into a transparent bulk ceramic via Current-Activated Pressure-Assisted Densification (CAPAD) as described previously [37]. The thickness of the resulting densified YSZ discs were reduced from 1 mm to ~300 µm by polishing with 30 µm diamond slurry on an automatic polisher (Pace Technologies, Tucson, Arizona USA). The samples were then polished with successively finer diamond and silica slurries ranging from 6 to 0.2 µm. Samples were sectioned into rectangles of approximately 2.1 x 2.2 mm using a diamond lapping saw (DTQ-5, WEIYI, Qingdao, China), followed by sonication in acetone and thorough rinsing in water. Optical transmittance and reflectance spectra for the polished implants are shown in Fig. 1.

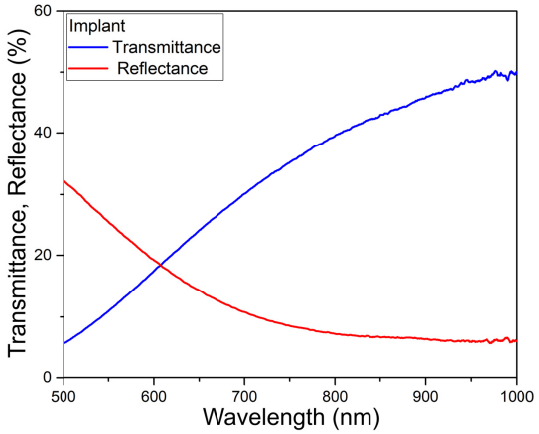


Fig. 1. Reflectance and transmittance spectra of Window to the Brain implant.

### 2.2 Animals

All experimental procedures and humane care of mice were conducted in compliance with the University of California, Riverside Institutional Animal Care and Use Committee approval. The N = 4 8-12-week-old C57Bl/6 male mice (Jackson Laboratory) used in this study were housed under a 12-hour light and 12-hour dark cycle with *ad libitum* access to food and water.

### 2.3 Surgical procedures

Craniectomy surgery was conducted as previously described [36]. Briefly, mice were anesthetized with isoflurane inhalation (0.2-0.5%), and given ketamine and xylazine (K/X) (80/10 mg/kg, i.p.). Additional anesthetic was administered as necessary. Hair was removed from the scalp using clippers and depilatory cream. Mice were then secured into stereotaxic frames to immobilize the head for surgery. Ophthalmic ointment was placed over the eyes, and the surgical site was sterilized with alternating application of betadine and 70% EtOH (3 times). Implants were also sterilized in 70% EtOH.

A sagittal incision was made to the left of the midline, and the scalp retracted to expose the skull. Periosteum was removed from the skull, and a craniectomy was performed with a surgical drill and carbide burr to remove a square section of skull over the right parietal lobe, with dimensions slightly larger than the implant. The YSZ implant was placed within the craniectomy directly on the intact *dura mater*, and dental cement was applied to each of the four corners of the implant to prevent displacement. Dental cement was cured with UV light exposure for 20 seconds. Figure 2(a) shows an illustration of implant placement envisioned in eventual human application, as well as implant placement used in mice in this study.

Imaging with LSI was conducted immediately after the cranioplasty procedure, while the scalp was still open, as well as follow-up imaging at 14 and 28 days (for Mice 1-3), or 60 days (for Mouse 4) after the implantation surgery. For each follow-up imaging procedure, mice were anesthetized as described above, and the scalp was reopened to expose the implant. Periosteum overlying the implant (and skull for Mouse 4) was removed, and imaging was conducted in an identical manner to the baseline imaging. During imaging sessions, small amounts of saline was dropped onto the skull periodically to prevent drying. Following each imaging procedure, the scalp was closed with continuous suture, and triple antibiotic ointment was applied to the surgical site. Buprenorphine was administered (0.1 mg/kg, s.c.) for postoperative pain control. Mice were placed on a heating pad to aid recovery from anesthesia. A second buprenorphine injection was administered between 4 and 6 hours after surgery.

### 2.4 Laser speckle imaging

LSI and regular images of regions of interest (ROI) (Fig. 2(c)) were acquired using a 12-bit CMOS camera (DCC1545M, Thorlabs, Newton, NJ, USA). For regular images, a diffuse IR source was used for illumination. For LSI, an 810 nm continuous wave NIR laser (Vari-Lase REF946, Vascular Solutions, Morrisville, NC, USA) was used to illuminate the ROI with incident power of 100 mW at a 45° incidence. While most LSI studies use visible wavelengths for illumination, we chose 810 nm to reduce reflectance and increase transmittance through the implant (see Fig. 1). The 810 nm laser intensity was homogenized using a diffuser (ED1-C20-MD, Thorlabs) and was expanded using a pair of negative-positive lenses (KPC043, –25 mm EFL and KPX094, 100 mm EFL, Newport, Irvine, CA, USA). Collimated laser light was shown onto the cortex through the WttB implant (i.e. ROI 1 in Mice 1-3) or through both skull and implant (i.e. ROI 1 and ROI 2 in Mouse 4). A sequence of laser speckle images reflected from each illuminated region was captured by the CMOS camera, which was focused 0.2 mm below the cortical surface using a 10X zoom microscope (MLH-10X, 152.4 mm WD, Computar, Torrance, CA, USA). For each ROI, a sequence of n = 100 images were captured at each of four different exposure times (1, 2, 6, and 10 ms) at a speed of 14 frames per second. The aperture and magnification of the zoom microscope were carefully chosen to ensure that the speckle size at the image plane was approximate to the area of a single pixel in the CMOS chip [9, 14, 18]. A schematic of the LSI system is shown in Fig. 2(b).

### 2.5 Experimental design

In this study, we conducted two separate experiments. Experiment 1 was conducted using mice 1-3, with LSI through the implant (i.e. ROI 1) at baseline immediately following implantation, and again after 14 and 28 days post-implantation. In Experiment 2, the LSI field of view was expanded to include both the implant (ROI 1) as well as native skull (ROI 2) in Mouse 4 at 60 days post-implantation. For both experiments, LSI imaging was conducted at 4 different exposure times. A timeline of imaging procedures for the two experiments is shown in Fig. 2(d).

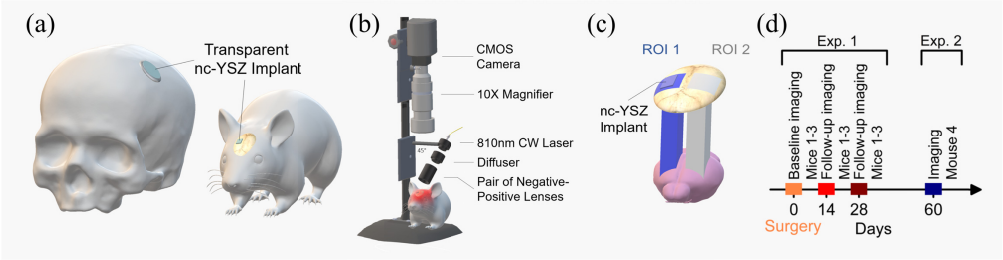


Fig. 2. a) Illustration of the Window to the Brain concept in human and mouse skulls, b) Schematic of the experimental imaging setup, c) Schematic of the craniotomy location on murine cranium and regions of interest: ROI 1, the nc-YSZ implant and ROI 2, the left parietal bone, d) Timeline for imaging procedures.

### 2.6 Image processing and data analysis

The contrast-resolved LSI images were constructed based on temporal statistical analysis of laser speckle which has been proven to preserve spatial resolution [14]. Experimental results have indicated that temporal speckle contrast analysis could expressively suppress the effect of the static laser speckle pattern formed by the stationary superficial reflection and scattering tissue on the visualization of blood flow [9, 14, 18–20]. Suppressing this effect makes temporal contrast analysis an ideal method for imaging cerebral blood flow through skull and

the transparent nc-YSZ implant. The temporal contrast, $K_t$, of each image pixel in the time sequence was calculated using Eq. (1) [9],

$$K_t(x,y) = \frac{\sigma_{(x,y)}}{\langle I_{(x,y)} \rangle} = \sqrt{\frac{1}{(N-1)} \left\{ \sum_{n=1}^{N} [I_{(x,y)}(n) - \langle I_{(x,y)} \rangle]^2 \right\}} \Big/ \langle I_{(x,y)} \rangle \quad (1)$$

where $I_{x,y}(n)$ is the intensity at pixel (x,y) in the nth image, N is the number of images acquired, and $\langle I_{x,y} \rangle$ is the mean value of intensity at pixel (x,y) over the N images.

We assessed the quality of the speckle contrast images over time in terms of signal to noise ratio (SNR) and vessel sharpness. To quantify signal to noise ratio for each exposure time and time point, the contrast intensity profile along a vertical line (across the blood vessels) was considered. The profile lines were chosen for each mouse such that 3 to 4 vessels were intersected, and remained the same between the time points and the exposure times. Figure 3(b) shows an example of the contrast intensity profile for 6 ms exposure time at day 0, 14 and 28 for Mouse 3. Equation (2) shows how SNR values were calculated for each exposure time and time point,

$$SNR = \Delta K / \sigma K_n \quad (2)$$

where $\Delta K$ is the depth of the vessel peak from the baseline (mean noise) and $\sigma K_n$ is the standard deviation of the noise. A visual example of $\Delta K$ and $\sigma K_n$ are shown in Fig. 3(b). The SNR values were averaged over the mice (1, 2, and 3) and standard errors were calculated. The optimum SNR between the exposure times in each time point was chosen for the contrast images sharpness comparison. As an indicator of resolution, we compared the sharpness of the vessel edges in images by calculating fall distance (the number of pixels) of the edge of the vessel to go from 10% to 90% of $\Delta K$ value were calculated [38]. A shorter fall distance corresponds to greater sharpness. The same sampled contrast intensity profiles were considered for the fall distance calculation. Figure 3(b) shows an example trace and 10–90% fall distance measurement. In order to evaluate the change in sharpness over the time points in Experiment 1, relative change in fall distance over the time points day 14 and day 28 compared to day 0 baseline for each animal and vessel were evaluated using Eq. (3).

$$Relative\ fall\ distance = \frac{Fall\ distance - Fall\ distance_{Day0}}{Fall\ distance_{Day0}} \quad (3)$$

To compare the blood vessel images through-skull and through-implant in Experiment 2, absolute fall distances with respect to the vessels size (FWHM) were determined. FWHM of the vessels in profiles were taken as the vessel diameter [39] (Fig. 3(b)).

## 3. Results

### *3.1 Experiment 1: LSI image quality over time*

The results from Experiment 1 are shown in Figs. 3 and 4. Figure 3(a) shows regular images and LSI temporal contrast images at each of the 4 exposure times, for days 0, 14 and 28 from Mouse 3 (data for Mice 1-2 not shown). In the regular images, some tissue regrowth is visible at the implant edges at 14 and 28 days. It should also be noted that at day 0, blood flow is expected to be altered in response to the invasive cranioplasty surgery (e.g. due to potential reactive hyperemia [40] (increased blood flow), changes in respiration, etc.). Due to these differences in the mouse biology and physiology at different imaging time points, we sought to determine the optimal exposure time for LSI imaging at each time point, so that we could compare the images of highest SNR that could be acquired at each time point.

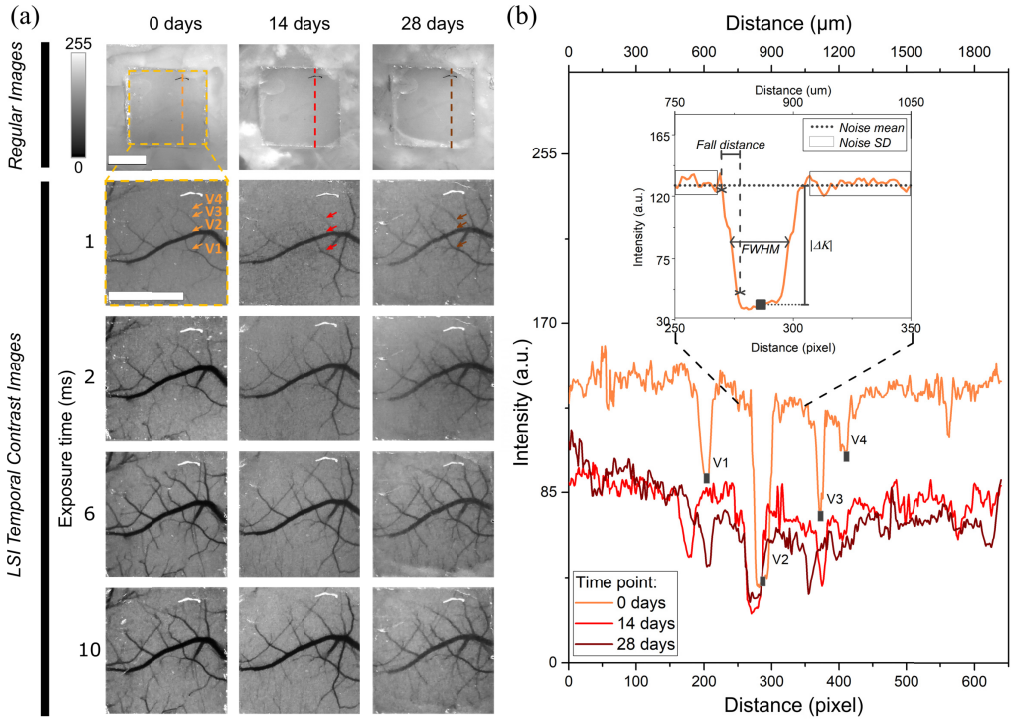


Fig. 3. a) Regular images and LSI images for exposure times of 1, 2, 6, and 10 ms, at 0, 14 and 28 days post-surgery from Mouse 3 (scale bars = 1 mm). b) Contrast intensity profiles of lines across the images (shown as a dashed line in panel a) at 0, 14 and 28 days post-surgery from Mouse 3. The arrows in a) show the vessels that are intersected by the profile lines shown in b), labeled as V1 through V4 in day 0 image and profile (V4 arrow was not shown in day 14 and day 28 since the microvessel is not visible). The inset in b) shows how noise parameters, |ΔK|, FWHM and fall distance are determined from the line profiles.

Line intensity profiles like the example shown in Fig. 3(b) were analyzed for all exposure times and imaging time points in Mice 1-3. From these intensity profiles, peak intensity and noise were determined (as described in the Methods section and illustrated in the inset of Fig. 3(b)), and signal-to-noise ratio (SNR) was calculated. Data for each time point and exposure time was averaged between the three mice, and is shown in Fig. 4(a). As shown in the figure, an exposure time of 6 ms gave the highest SNR at 0 and 28 days, while 10 ms exposure time gave a higher SNR at 14 days.

Next, using the 9 LSI temporal contrast images corresponding to these optimal exposure times for days 0, 14 and 28 for Mice 1-3, we sought to compare the sharpness (i.e. fall distance) of the vessels in the images to determine if the images were becoming blurred and losing resolution over time since implantation. The relative change in fall distance between days 14 and 28 compared to day 0 baseline are shown in Fig. 4(b), and was below a 13% increase for all vessels analyzed. On average, relative fall distance increased by 6.56% ± 1.03% by day 14, and 7.69% ± 1.2% by day 28 compared to day 0.

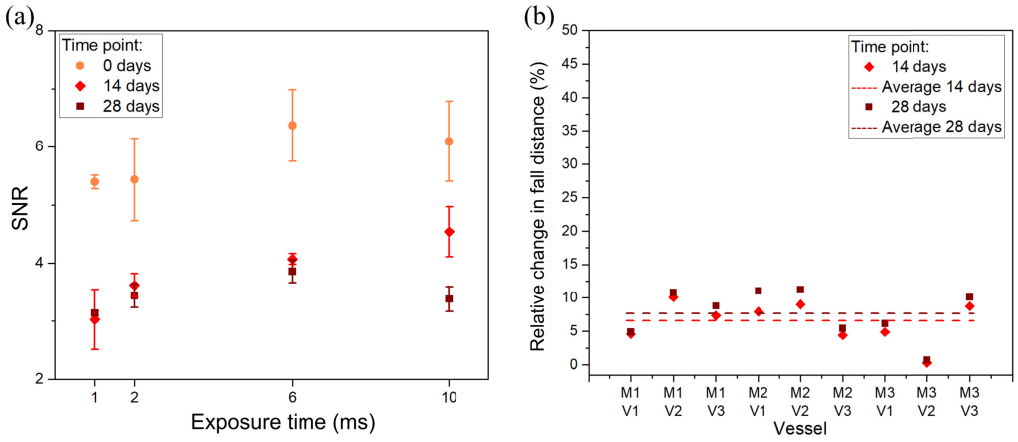


Fig. 4. a) SNR for different exposure times and imaging time points (mean and standard error) and b) Relative change in fall distance between days 14 and 28 vs day 0 for 3 vessels each of Mice 1-3 (dashed lines represent mean change i5n fall distance for all 9 vessels).

### *3.2 Experiment 2: LSI image quality through skull vs. chronic implant*

As the goal of the WttB implant is to provide long-term optical access to the brain for imaging techniques such as LSI, we sought to compare LSI imaging through the native skull with imaging through a chronic implant which had been in the body long term. Thus, in Experiment 2, Mouse 4 was imaged with LSI 60 days post-implantation. To make a direct comparison between the implant and skull, the LSI field of view was expanded to include both ROI 1 (the implant over the right parietal lobe) and ROI 2 (corresponding region of skull over the left parietal lobe) in the same image. Figure 5(a) shows the LSI temporal contrast images for exposure times of 1, 2, 6 and 10 ms.

Unlike Experiment 1, where a given field of view was compared with itself over time, Experiment 2 compares two separate regions of the brain with different vessels. Thus, for this second experiment, 3 line profiles with taken for the implant and for the corresponding region of skull. To avoid selection bias, the location of these line profiles were chosen arbitrarily at the ROI mid- and quarter-points, as depicted in the regular image in Fig. 5(b). As an example, Fig. 5(c) shows the intensity profiles from the midline of both ROI 1 and ROI 2 for exposure time 6 ms.

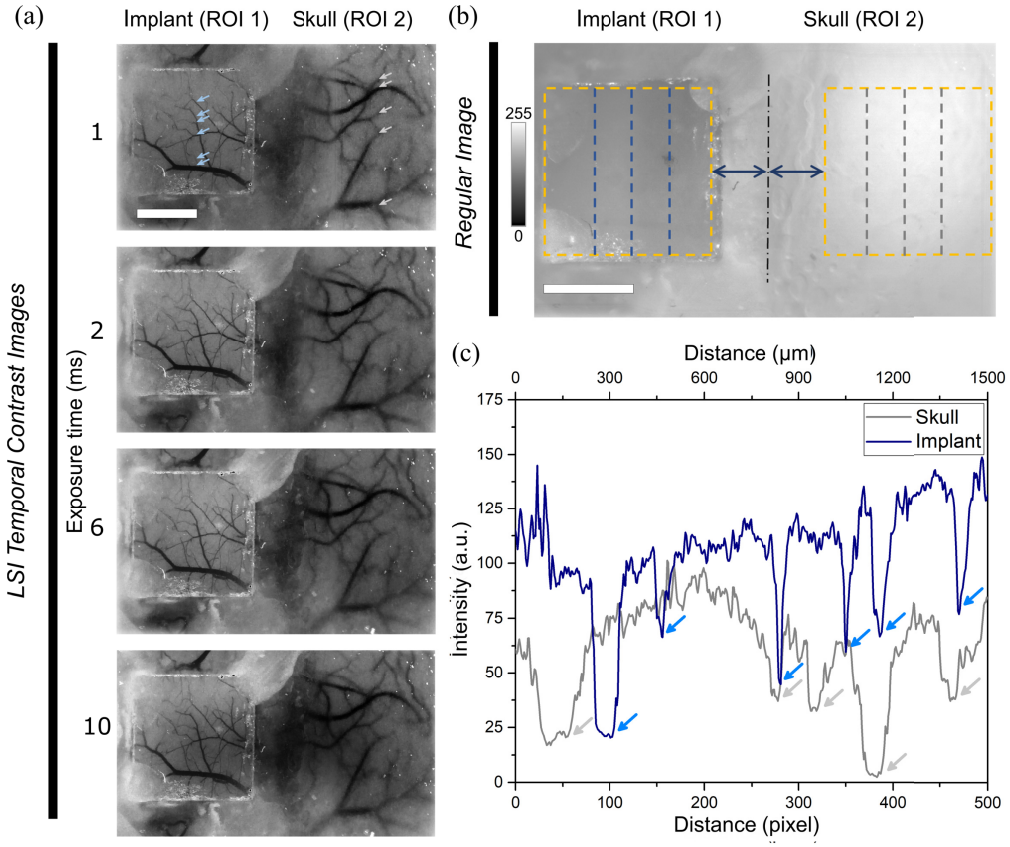


Fig. 5. a) LSI temporal contrast images for 4 exposure times in Mouse 4. The left side of each image is the WttB implant (ROI 1), and ROI 2 is the corresponding region of skull on the right side of each image. b) Regular image of implant, showing the arbitrary locations where line profiles were taken. c) Example contrast intensity profiles along the midline of ROI 1 and 2 for exposure time 6 ms. The arrows in a) and c) show the vessels that are intersected by the midline intensity profiles. Scale bars = 1 mm.

Using the same analysis methods described in Experiment 1, we calculated the SNR from each line profile in ROI 1 and ROI 2 for each exposure time. The mean SNR for each exposure time is shown in Fig. 6(a). The 6 ms exposure time LSI temporal contrast image resulted in the highest SNR for both implant and skull, and thus we used this image to compare the SNR and sharpness of detected vessels by LSI between native skull and a long-term WttB implant. By the same method used in Experiment 1, we analyzed the 3 line profiles across the WttB implant and 3 line profiles across the skull to determine the fall distance and SNR for each vessel. Additionally, the full-width half-max (FWHM) of each vessel in the line profiles were taken as vessel diameter [33]. Figure 6(b) shows a plot of all vessels intersected by the 6 profile lines, with SNR plotted against FWHM (i.e. vessel diameter). A plot of all vessels intersected by the 6 profile lines, with absolute fall distance (i.e. vessel sharpness) plotted against FWHM (i.e. vessel diameter) is shown in Fig. 6c.

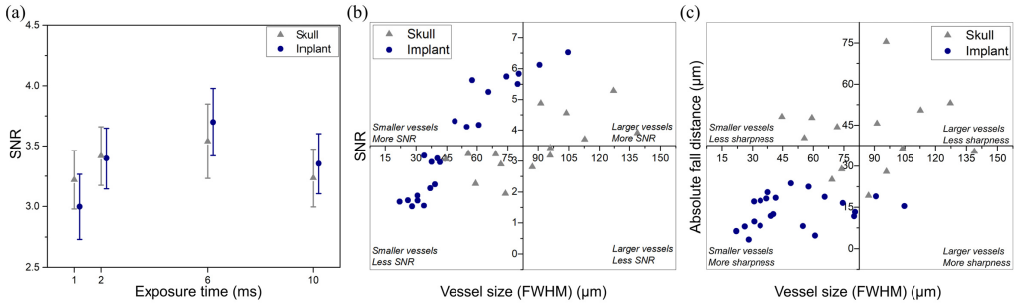


Fig. 6. a) Mean SNR of contrast intensity along arbitrary line profiles on the implant and skull for 4 separate exposure times (error bars represent standard error), b) and c) SNR and sharpness (respectively) vs FWHM for all vessels intersected by arbitrary line profiles on the implant and skull for the LSI temporal contrast image acquired with 6 ms exposure time.

## 4. Discussion

The WttB holds the transformative potential for facilitating diagnosis and treatment of a wide variety of brain pathologies and neurological disorders. We envision this implant having the potential to enable delivery to and/or acquisition of light from the brain, in real-time, without the need for repeated highly-invasive craniotomies. Such access may also create a new platform for understanding the brain. As the goal of the WttB implant is to provide this access long-term, it is important that the optical access is not lost over time. In this study, we assessed LSI temporal contrast imaging quality (i.e. sharpness) of cerebral blood vessels imaged through the implant up to 60 days post-implantation.

In LSI temporal contrast imaging, the exposure time of the camera can have a large effect on image quality. As exposure time increases, both the contrast intensity and noise of the image increase [21]. While the contrast plateaus after some threshold, noise continues to increase with exposure time. Several sources of noise contribute to the measured noise, including physiological noise, hardware noise, environmental noise, and noise due to statistical uncertainties. The total noise of the speckle contrast signal is a combination of all of these sources and the relative contributions of each of these exhibit different characteristics with respect to the exposure time [21]. However, in our experiments, the physiologic noise (including noise due to implantation surgery) is the dominant source because it is the only one that is changing considerably over time. Physiologic noise arises from motion of the tissue such as heartbeat or respiration-induced pulsatile motion of the exposed cortex, baseline fluctuations in the cerebral blood flow, and possibly tissue regrowth and revascularization following implantation. This motion and blood flow fluctuations introduce additional velocity components to the measured signal and therefore cause speckle contrast fluctuations. Since the physiological noises will be different on different days, exposure time should be optimized during each imaging session. To determine the optimal exposure time in this study, we compared the SNR of images taken at exposure times of 1, 2, 6, and 10 ms (Fig. 4(a), Fig. 6(a)), and each imaging session proceeded with the exposure time that maximized SNR. Indeed, our results found that the optimal exposure time differed between the imaging time points in Experiment 1, with maximum SNR for exposure time of 6 ms at days 0 and 28, and 10 ms at day 14. This may be explained by the differences in physiology between these time points. At day 0, altered blood flow due to the implantation surgery is expected, and elevated blood flow could give high contrast to the vessels. Thus, a lower exposure time (6 ms) can provide sufficient contrast of the blood flow, while keeping noise low. By day 14, flow would no longer be modified in response to the surgery, and thus a higher exposure time (10 ms) may be needed to increase contrast in the images. At time points beyond 14 days, flow remains low compared to day 0, but noise may increase due to healing processes (tissue regrowth, revascularization, etc.), and thus a shorter exposure time (6 ms) may provide the

best compromise between increased contrast and reduced noise. It should be noted, however, that the modification of blood flow at the different time points, as evidenced by the different optimal exposure times, may also be due to several other confounding factors. Anesthetic agents (including isoflurane and ketamine used in this study) are known to modulate cerebral blood flow, and the concentration of these drugs in the blood stream was not kept constant over the imaging sessions. Respiration can cause noise in LSI, and its rate, along with arterial blood gas levels, can significantly alter blood flow. These variables, in addition to the small sample size used in this study, make it difficult to attribute the observed differences in blood flow between the time points to a particular cause.

Image resolution (i.e. sharpness) was found to decrease by up to 13% over the 28 days compared to day 0 baseline in the 9 vessels analyzed from Mice 1-3 (Fig. 4(b)). The relative increases in average fall distance between day 14 and day 28 compared to day 0 were 6.56% ± 1.03% and 7.69% ± 1.2%, respectively. It should be noted that while day 0 is considered as the baseline for comparison, it does not represent an unperturbed state of normal cerebral blood flow. It is likely that blood flow was altered in response to the invasive cranioplasty surgery, and thus the higher SNR and sharpness of the day 0 images compared with days 14 and 28 may be due in part to an elevated signal at day 0, rather than a loss of signal at days 14 and 28. SNR and sharpness stayed more stable between 14 and 28 days, consistent with this hypothesis. Additionally, new microvessels which were not visible in day 0 are visible at these later time points, which suggests revascularization may be occurring near the implant surface. Together, these results appear to indicate that image quality remains high up to 28 days post-implantation, but additional longer time points are needed to confirm this is the case. In Experiment 2, a day 60 time point shows that SNR is similar to the SNRs obtained at days 14 and 28 in Experiment 1 (SNR between 3 to 4 in both Fig. 4(a) and Fig. 6(a)), and microvessels are clearly visible at this later time point (Fig. 5(a)).

Comparing imaging through the skull and a long-term (60 days) implant (Fig. 5(a)), the skull had a higher SNR for lower exposure times (1 and 2 ms), and the implant SNR was higher at longer exposure times (6 and 10 ms) (Fig. 6(a)). The higher SNR of the through-skull images compared with implant at short exposure times may be explained by the natural filtering-out of smaller vessels imaged through the skull. Imaging through the window, on the other hand, resolves small vessels which are more sensitive to exposure time. At low exposure time, the contrast of these small vessels is very low, contributing to the lower SNR through the window compared to skull. Exposure time of 6 ms gave the highest SNR for both skull and implant and was used for comparing SNR and sharpness of vessels imaged beneath each. Because this comparison was made between two different spatial regions of the brain, different vessels of varying diameter were compared. Thus, SNR and sharpness of vessels (fall distance) are plotted against the vessel diameter (FWHM of vessels in intensity profiles). As mentioned earlier a number of small vessels, associated with lower blood flow and accordingly SNR, were detected through the implant which were naturally filtered-out by the skull (Fig. 6(b)). These detected small vessels decreased the averaged SNR shown in Fig. 6(a). In Fig. 6(c), interestingly, the data from the skull and implant fell into separate clusters, with vessels imaged through the implant having smaller FWHM and shorter fall distances, while vessels imaged through the skull have larger FWHM and higher fall distances. This data shows that vessels imaged through the implant appear smaller in diameter and have sharper borders compared to those imaged through the skull. As the size of vessels and velocity of blood flow is not expected to differ on average between the two hemispheres of the mouse brain, the apparent increase in vessel diameter imaged through the skull vs implant is likely due to blurring of the image through the skull. In general, the light transmission to the brain and reflection from the brain are lower in the through-skull image. Additionally, the skull scattering disorders the speckle pattern that was created by the brain hemodynamics, making a less accurate speckle pattern. Both of the defects are caused by skull and the skull texture is not homogeneous, making image correction or enhancement very complex [14].

The reduction in border sharpness of the vessels imaged through the skull vs implant is consistent with this explanation, and the blurred nature of the through-skull image compared to the through-implant image is visually apparent in Fig. 5(a). It should also be noted that while the SNR and sharpness of the through-implant images are an improvement over the through-skull images, the mouse skull is inherently transparent itself [14], which is not the case in larger animals or humans.

LSI temporal contrast imaging has become a useful tool for brain blood flow applications as the images it produces contain functional information (i.e. relative blood velocity) in addition to showing structure of the vessel networks. Figure 7 contains a color map version of the 6 ms LSI image from Mouse 4 (Fig. 5(a)), where minimum relative velocity (i.e. static regions) appears blue and maximum relative velocity (i.e. maximum blood flow velocity) appears red. As seen in Fig. 7, much more precise velocity information, particularly of microvessels, can be detected through the implant, while the reduced sharpness of the vessels imaged through skull obscures precise flow determinations. Imaging microvessels (usually involving small arteries of less than 150 μm in diameter, arterioles, capillaries, and venules [41, 42]) is important for many applications, as microcirculation plays a critical role in physiological processes such as tissue oxygenation and nutritional exchange [43]. Monitoring the spatio-temporal characteristics of microcirculation is crucial for studying the normal and pathophysiologic conditions of tissue metabolism. It is also useful for assessing microcirculatory dysfunction due to disease conditions such as type 2 diabetes, peripheral vascular disease (PVD), atherosclerotic coronary artery disease, obesity, heart failure, Alzheimer's, schizophrenia and hypertension, among others [44–46]. In addition, quantification of dynamic blood flow, angiogenesis, and vessel density are critical for monitoring the progression of wound healing [47]. Although high resolution vascular network mapping is possible using imaging modalities such as computed tomography (CT), these approaches require injection of contrast agents and pose disadvantages such as radiation exposure. Existing non-invasive methodologies (including LSI through skull) are inadequate to study blood flow at microvessel resolution [48]. Windows such as the WttB implant are thus important tools for research, and in the case of the WttB implant, can become important enablers of clinical diagnostics and therapy involving cerebral microvessels.

As recent studies show, creating novel windows for brain studies has been gaining attention recently [25, 49–51]. Some of these studies, involving optical clearing agents (OCAs) applied to the scalp overlying native skull, have shown limited success due to optical losses and scattering in the skull. These skin optical clearing strategies could work in conjunction with the WttB implant, to allow for imaging of cerebral blood flow in awake and behaving animals through closed scalp and implant, for example to study cerebrovascular hemodynamic responses and tissue oxygenation and other stimuli. Future studies by our group will explore this combined OCA-WttB strategy, as well as including additional imaging modalities which can couple with LSI to provide additive information, such as OCT and intrinsic optical signal (IOS).

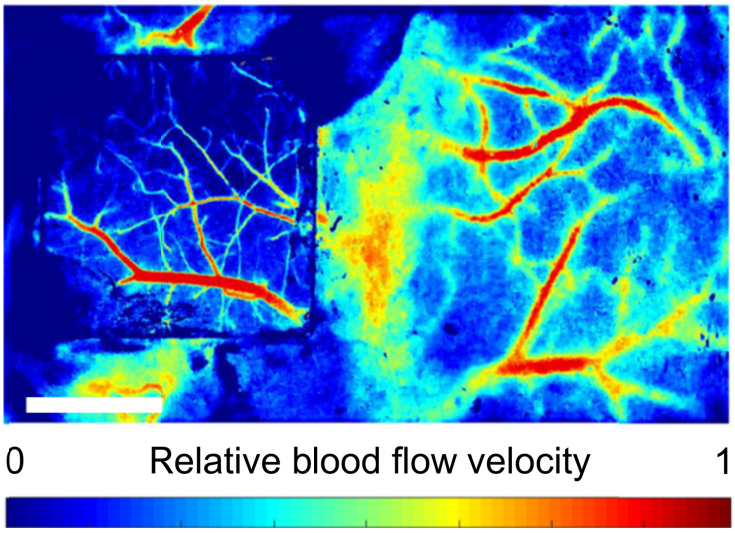


Fig. 7. Relative blood flow velocity in the 6 ms exposure time LSI temporal contrast image from Mouse 4. Scale bar = 1 mm.

There are several limitations to the current study. The sample sizes used were small (n = 3 and n = 1), and further experiments are needed to confirm the reproducibility of these findings. While a permanent cranial implant can allow for less invasive imaging of the brain at later time points, it requires an initial implantation surgery which carries associated risks such as infection.

## 5. Conclusion

In conclusion, the Window to the Brain implant was found to remain stable for LSI imaging up to 28 days, with average relative change in vessel sharpness under 8%. An additional imaging session at 60 days found improved sharpness and visibility of microvessels compared to imaging through skull which blurred and distorted vessels. These results suggest that this implant can provide long-term access for brain imaging, but longer term studies are needed.

## Funding

National Science Foundation (NSF-PIRE) (1545852) and "Beca Mixta" from National Council of Science and Technology of Mexico (CONACYT) (741249).

## Acknowledgments

Portions of this work were presented at SPIE Photonics West, San Francisco, CA in 2018, Vol. 10493, p. 1049303 [36].

## Disclosures

The authors declare that there are no conflicts of interest related to this article.

## References

1. T. Asakura and N. Takai, "Dynamic laser speckles and their application to velocity measurements of the diffuse object," Appl. Phys. (Berl.) **25**(3), 179–194 (1981).
2. H. Fujii, K. Nohira, Y. Yamamoto, H. Ikawa, and T. Ohura, "Evaluation of blood flow by laser speckle image sensing. Part 1," Appl. Opt. **26**(24), 5321–5325 (1987).
3. S. J. Rothberg and B. J. Halkon, "Laser vibrometry meets laser speckle," in *Sixth International Conference on Vibration Measurements by Laser Techniques: Advances and Applications*, (SPIE, 2004), 12.
4. H. Fujii, T. Asakura, and Y. Shindo, "Measurement of surface roughness properties by using image speckle contrast," J. Opt. Soc. Am. **66**(11), 1217–1222 (1976).

5. M. X. Tang, D. S. Elson, R. Li, C. Dunsby, and R. J. Eckersley, "Photoacoustics, thermoacoustics, and acousto-optics for biomedical imaging," Proc. Inst. Mech. Eng. H **224**(2), 291–306 (2010).
6. J. Li, G. Ku, and L. V. Wang, "Ultrasound-modulated optical tomography of biological tissue by use of contrast of laser speckles," Appl. Opt. **41**(28), 6030–6035 (2002).
7. J. D. Briers and S. Webster, "Laser speckle contrast analysis (LASCA): a nonscanning, full-field technique for monitoring capillary blood flow," J. Biomed. Opt. **1**(2), 174–179 (1996).
8. A. K. Dunn, H. Bolay, M. A. Moskowitz, and D. A. Boas, "Dynamic imaging of cerebral blood flow using laser speckle," J. Cereb. Blood Flow Metab. **21**(3), 195–201 (2001).
9. H. Cheng, Q. Luo, S. Zeng, S. Chen, J. Cen, and H. Gong, "Modified laser speckle imaging method with improved spatial resolution," J. Biomed. Opt. **8**(3), 559–564 (2003).
10. Q. Liu, Z. Wang, and Q. Luo, "Temporal clustering analysis of cerebral blood flow activation maps measured by laser speckle contrast imaging," J. Biomed. Opt. **10**(2), 024019 (2005).
11. D. A. Boas and A. K. Dunn, "Laser speckle contrast imaging in biomedical optics," J. Biomed. Opt. **15**(1), 011109 (2010).
12. J. D. Briers, "Laser speckle contrast imaging for measuring blood flow," Opt. Appl. **37**, 1 (2007).
13. N. Konishi and H. Fujii, "Real-time visualization of retinal microcirculation by laser flowgraphy," in *Optical Engineering,* Vol. 38 (SPIE, 1995), 5.
14. P. Li, S. Ni, L. Zhang, S. Zeng, and Q. Luo, "Imaging cerebral blood flow through the intact rat skull with temporal laser speckle imaging," Opt. Lett. **31**(12), 1824–1826 (2006).
15. A. B. Parthasarathy, S. M. Kazmi, and A. K. Dunn, "Quantitative imaging of ischemic stroke through thinned skull in mice with Multi Exposure Speckle Imaging," Biomed. Opt. Express **1**(1), 246–259 (2010).
16. A. Y. Shih, C. Mateo, P. J. Drew, P. S. Tsai, and D. Kleinfeld, "A polished and reinforced thinned-skull window for long-term imaging of the mouse brain," J. Vis. Exp. **61**, 3742 (2012).
17. J. Wang, Y. Zhang, T. H. Xu, Q. M. Luo, and D. Zhu, "An innovative transparent cranial window based on skull optical clearing," Laser Phys. Lett. **9**(6), 469–473 (2012).
18. N. Li, X. Jia, K. Murari, R. Parlapalli, A. Rege, and N. V. Thakor, "High spatiotemporal resolution imaging of the neurovascular response to electrical stimulation of rat peripheral trigeminal nerve as revealed by in vivo temporal laser speckle contrast," J. Neurosci. Methods **176**(2), 230–236 (2009).
19. D. Zhu, J. Wang, Z. Zhi, X. Wen, and Q. Luo, "Imaging dermal blood flow through the intact rat skin with an optical clearing method," J. Biomed. Opt. **15**(2), 026008 (2010).
20. W. Chen, K. Park, N. Volkow, Y. Pan, and C. Du, "cocaine-induced abnormal cerebral hemodynamic responses to forepaw stimulation assessed by integrated multi-wavelength spectroimaging and laser speckle contrast imaging," IEEE J. Sel. Top Quantum Electron. **22**, 6802608 (2016).
21. S. Yuan, A. Devor, D. A. Boas, and A. K. Dunn, "Determination of optimal exposure time for imaging of blood flow changes with laser speckle contrast imaging," Appl. Opt. **44**(10), 1823–1830 (2005).
22. Y. Aizu, H. Ambar, T. Yamamoto, and T. Asakura, "Measurements of flow velocity in a microscopic region using dynamic laser speckles based on the photon correlation," Opt. Commun. **72**(5), 269–273 (1989).
23. C. J. Roome and B. Kuhn, "Chronic cranial window with access port for repeated cellular manipulations, drug application, and electrophysiology," Front. Cell. Neurosci. **8**, 379 (2014).
24. V. Zuluaga-Ramirez, S. Rom, and Y. Persidsky, "Craniula: A cranial window technique for prolonged imaging of brain surface vasculature with simultaneous adjacent intracerebral injection," Fluids Barriers CNS **12**(1), 24 (2015).
25. C. Heo, H. Park, Y. T. Kim, E. Baeg, Y. H. Kim, S. G. Kim, and M. Suh, "A soft, transparent, freely accessible cranial window for chronic imaging and electrophysiology," Sci. Rep. **6**(1), 27818 (2016).
26. S. S. Smith, P. Magnusen, and B. J. Pletka, "Fracture toughness of glass using the indentation fracture technique," *Fracture Mechanics for Ceramics, Rocks, and Concrete* (ASTM International) (1981).
27. S. F. Hulbert, "The use of alumina and zirconia in surgical implants," An Introduction to Bioceramics **1**, 25–40 (1993).
28. Y. Damestani, C. L. Reynolds, J. Szu, M. S. Hsu, Y. Kodera, D. K. Binder, B. H. Park, J. E. Garay, M. P. Rao, and G. Aguilar, "Transparent nanocrystalline yttria-stabilized-zirconia calvarium prosthesis," Nanomedicine (Lond.) **9**(8), 1135–1138 (2013).
29. Y. Damestani, D. E. Galan-Hoffman, D. Ortiz, P. Cabrales, and G. Aguilar, "Inflammatory response to implantation of transparent nanocrystalline yttria-stabilized zirconia using a dorsal window chamber model," Nanomedicine (Lond.) **12**(7), 1757–1763 (2016).
30. J. E. Alaniz, F. G. Perez-Gutierrez, G. Aguilar, and J. E. Garay, "Optical properties of transparent nanocrystalline yttria stabilized zirconia," Opt. Mater. **32**(1), 62–68 (2009).
31. S. R. Casolco, J. Xu, and J. E. Garay, "Transparent/translucent polycrystalline nanostructured yttria stabilized zirconia with varying colors," Scr. Mater. **58**(6), 516–519 (2008).
32. P. Christel, A. Meunier, M. Heller, J. P. Torre, and C. N. Peille, "Mechanical properties and short-term in-vivo evaluation of yttrium-oxide-partially-stabilized zirconia," J. Biomed. Mater. Res. **23**(1), 45–61 (1989).
33. K. Nakamura, T. Kanno, P. Milleding, and U. Ortengren, "Zirconia as a dental implant abutment material: a systematic review," Int. J. Prosthodont. **23**(4), 299–309 (2010).
34. P. Christel, A. Meunier, J. M. Dorlot, J. M. Crolet, J. Witvoet, L. Sedel, and P. Boutin, "Biomechanical compatibility and design of ceramic implants for orthopedic surgery," Ann. N. Y. Acad. Sci. **523**(1 Bioceramics), 234–256 (1988).

35. M. I. Gutierrez, E. H. Penilla, L. Leija, A. Vera, J. E. Garay, and G. Aguilar, "Novel Cranial Implants of Yttria-Stabilized Zirconia as Acoustic Windows for Ultrasonic Brain Therapy," Adv. Healthc. Mater. **6**(21), 1700214 (2017).
36. N. Davoodzadeh, D. Halaney, C. R. Jonak, N. Cuando, A. Aminfar, D. K. Binder, and G. Aguilar, "Laser speckle imaging of brain blood flow through a transparent nanocrystalline yttria-stabilized-zirconia cranial implant," in *SPIE BiOS*, (SPIE, 2018), 7.
37. J. E. Garay, "Current-Activated, Pressure-Assisted Densification of Materials," Annu. Rev. Mater. Res. **40**(1), 445–468 (2010).
38. M. Fauver, E. Seibel, J. R. Rahn, M. Meyer, F. Patten, T. Neumann, and A. Nelson, "Three-dimensional imaging of single isolated cell nuclei using optical projection tomography," Opt. Express **13**(11), 4210–4223 (2005).
39. E. B. Hutchinson, B. Stefanovic, A. P. Koretsky, and A. C. Silva, "Spatial flow-volume dissociation of the cerebral microcirculatory response to mild hypercapnia," Neuroimage **32**(2), 520–530 (2006).
40. J. K. Gourley and D. D. Heistad, "Characteristics of reactive hyperemia in the cerebral circulation," Am. J. Physiol. **246**(1), H52–H58 (1984).
41. M. Roustit and J. L. Cracowski, "Assessment of endothelial and neurovascular function in human skin microcirculation," Trends Pharmacol. Sci. **34**(7), 373–384 (2013).
42. D. Rizzoni, C. Aalkjaer, C. De Ciuceis, E. Porteri, C. Rossini, C. A. Rosei, A. Sarkar, and E. A. Rosei, "How to assess microvascular structure in humans," High Blood Press. Cardiovasc. Prev. **18**(4), 169–177 (2011).
43. S. C. Gnyawali, K. Blum, D. Pal, S. Ghatak, S. Khanna, S. Roy, and C. K. Sen, "Retooling laser speckle contrast analysis algorithm to enhance non-invasive high resolution laser speckle functional imaging of cutaneous microcirculation," Sci. Rep. **7**(1), 41048 (2017).
44. F. G. R. Fowkes, D. Rudan, I. Rudan, V. Aboyans, J. O. Denenberg, M. M. McDermott, P. E. Norman, U. K. A. Sampson, L. J. Williams, G. A. Mensah, and M. H. Criqui, "Comparison of global estimates of prevalence and risk factors for peripheral artery disease in 2000 and 2010: a systematic review and analysis," Lancet **382**(9901), 1329–1340 (2013).
45. L. A. Sokolnicki, S. K. Roberts, B. W. Wilkins, A. Basu, and N. Charkoudian, "Contribution of nitric oxide to cutaneous microvascular dilation in individuals with type 2 diabetes mellitus," Am. J. Physiol. Endocrinol. Metab. **292**(1), E314–E318 (2007).
46. Z. Khalil, D. LoGiudice, B. Khodr, P. Maruff, and C. Masters, "Impaired peripheral endothelial microvascular responsiveness in Alzheimer's disease," J. Alzheimers Dis. **11**(1), 25–32 (2007).
47. S. C. Gnyawali, K. G. Barki, S. S. Mathew-Steiner, S. Dixith, D. Vanzant, J. Kim, J. L. Dickerson, S. Datta, H. Powell, S. Roy, V. Bergdall, and C. K. Sen, "High-resolution harmonics ultrasound imaging for non-invasive characterization of wound healing in a pre-clinical swine model," PLoS One **10**(3), e0122327 (2015).
48. S. Eriksson, J. Nilsson, and C. Sturesson, "Non-invasive imaging of microcirculation: a technology review," Med. Devices (Auckl.) **7**, 445–452 (2014).
49. K. Kisler, D. Lazic, M. D. Sweeney, S. Plunkett, M. El Khatib, S. A. Vinogradov, D. A. Boas, S. Sakadži, and B. V. Zlokovic, "In vivo imaging and analysis of cerebrovascular hemodynamic responses and tissue oxygenation in the mouse brain," Nat. Protoc. **13**(6), 1377–1402 (2018).
50. A. Holtmaat, T. Bonhoeffer, D. K. Chow, J. Chuckowree, V. De Paola, S. B. Hofer, M. Hübener, T. Keck, G. Knott, W. C. Lee, R. Mostany, T. D. Mrsic-Flogel, E. Nedivi, C. Portera-Cailliau, K. Svoboda, J. T. Trachtenberg, and L. Wilbrecht, "Long-term, high-resolution imaging in the mouse neocortex through a chronic cranial window," Nat. Protoc. **4**(8), 1128–1144 (2009).
51. I. Costantini, J. P. Ghobril, A. P. Di Giovanna, A. L. Allegra Mascaro, L. Silvestri, M. C. Müllenbroich, L. Onofri, V. Conti, F. Vanzi, L. Sacconi, R. Guerrini, H. Markram, G. Iannello, and F. S. Pavone, "A versatile clearing agent for multi-modal brain imaging," Sci. Rep. **5**(1), 9808 (2015).